energies

MDPI

Article

A Viscoplasticity Model for Shale Creep Behavior and Its Application on Fracture Closure and Conductivity

Shiyuan Li [1,2,*], Jingya Zhao [2], Haipeng Guo [1,3], Haigang Wang [1,3], Muzi Li [1,3], Mengjie Li [2], Jinquan Li [2] and Junwang Fu [2]

[1] Hebei Cangzhou Groundwater and Land Subsidence National Observation and Research Station, Cangzhou 061000, China; guohaipeng@mail.cgs.gov.cn (H.G.); wanghaigang@mail.cgs.gov.cn (H.W.); limuzi@mail.cgs.gov.cn (M.L.)
[2] School of Petroleum Engineering, China University of Petroleum-Beijing, Beijing 102249, China; zjy08310@163.com (J.Z.); limengjie0330@163.com (M.L.); liaucho@outlook.com (J.L.); fujunwang2001@163.com (J.F.)
[3] China Institute of Geo-Environment Monitoring, Beijing 100081, China
* Correspondence: lishiyuan1983@cup.edu.cn

Abstract: Hydraulic fracturing is the main means for developing low-permeability shale reservoirs. Whether to produce artificial fractures with sufficient conductivity is an important criterion for hydraulic fracturing evaluation. The presence of clay and organic matter in the shale gives the shale creep, which makes the shale reservoir deform with time and reduces the conductivity of the fracture. In the past, the influence of shale creep was ignored in the study of artificial fracture conductivity, or the viscoelastic model was used to predict the conductivity, which represents an inaccuracy compared to the actual situation. Based on the classical Perzyna viscoplastic model, the elasto-viscoplastic constitutive model was obtained by introducing isotropic hardening, and the model parameters were obtained by fitting the triaxial compression creep experimental data under different differential stresses. Then, the constitutive model was programmed in a software platform using the return mapping algorithm, and the model was verified through the numerical simulation of the triaxial creep experiment. Then, the creep calculation results of the viscoplastic constitutive model and the power law model were compared. Finally, the viscoplastic constitutive model was applied to the simulation of the long-term conductivity of the fracture to study the influence of creep on the fracture width, and sensitivity analysis of the influencing factors of the fracture width was carried out. The results show that the numerical calculation results of the viscoplastic model were in agreement with the experimental data. The decrease in fracture width caused by pore pressure dissipation and reservoir creep after 72 h accounts for 32.07% of the total fracture width decrease.

Keywords: viscoplasticity; creep behavior; fracture closure

Citation: Li, S.; Zhao, J.; Guo, H.; Wang, H.; Li, M.; Li, M.; Li, J.; Fu, J. A Viscoplasticity Model for Shale Creep Behavior and Its Application on Fracture Closure and Conductivity. *Energies* **2024**, *17*, 1122. https://doi.org/10.3390/en17051122

Academic Editors: Reza Rezaee, Hai Sun, Wenchao Liu and Daobing Wang

Received: 24 January 2024
Revised: 19 February 2024
Accepted: 23 February 2024
Published: 27 February 2024

1. Introduction

In the current context of "carbon peak" and "carbon neutrality", the demand for natural gas as a clean and low-carbon fossil fuel is gradually increasing [1]. As an important source of natural gas, shale has attracted increasing attention [2], and pores and natural micro-fractures of shale are the main reservoir space of shale gas. However, shale has extremely low porosity and permeability [3], usually ranging from millidarcy to nanodarcy, and must be fractured to create complex artificial fracture networks to form effective productivity. The key to hydraulic fracturing is determining whether a fracture with high conductivity can be formed. The presence of clay and organic matter in the shale gives the shale creep [4,5]. The proppants in the fracture are embedded in the shale reservoirs due to shale elastic and creep deformation during the production of shale gas, which causes fracture closure and long-term conductivity loss [6–8].

A large number of creep experiment results using shale show that the majority of the creep deformation is unrecoverable plastic deformation [9–11]. For example, Sone and Zoback conducted a creep experiment with unloading/reloading differential stress paths using a Haynesville shale sample, and the results showed that there is a significant plastic component in the strain response [11]. Chang and Zoback conducted a laboratory experiment on room-dried unconsolidated GOM shale under hydrostatic pressure and triaxial compressive stress, and the results showed that shale exhibits negligible creep strain accompanying unloading [9]. Therefore, it is appropriate to use the viscoplastic model to describe shale creep.

There are two commonly used viscoplastic theories. One is the Perzyna model, and the other is the Duvaut–Lions model. In 2020, Borja pointed out that the two models can obtain similar creep results when the two models' material parameters are selected appropriately [12]. Figure 1 shows the creep strain responses calculated by the Perzyna and Duvaut–Lions model when adjusting the ratio η/τ, η is the viscosity of the shale rock and τ is the relaxation time. Since Perzyna proposed the elastic–viscoplastic theoretical framework in 1963, many scholars have extended it to form their constitutive models and applied them to engineering practice. In 2010, Chang combined the Perzyna viscoplastic constitutive law with a modified Cambridge clay plastic yield model to describe the viscoplastic behavior of room-dried shale [13]. In 2012, Darabi used the classical Perzyna viscoplastic model to predict the mechanical response of asphalt concrete under cyclic loading and unloading creep test and found that with the increase in the number of cycles, the predicted value of the model significantly deviated from the experimental data, so the viscoplastic-softening model was proposed [14]. In 2020, Kabwe replaced the Newtonian element with a spring-pot in the Maxwell and VP components and obtained the fraction-order derivative viscoelastic viscoplastic (FDVP) model to estimate the delayed deformation characterized by squeezing [15]. In 2020, Haghighat developed a viscoplastic model to reproduce creep behavior and inelastic deformation by combining the Perzyna-type viscoplastic model and the modified Cam-clay model [16].

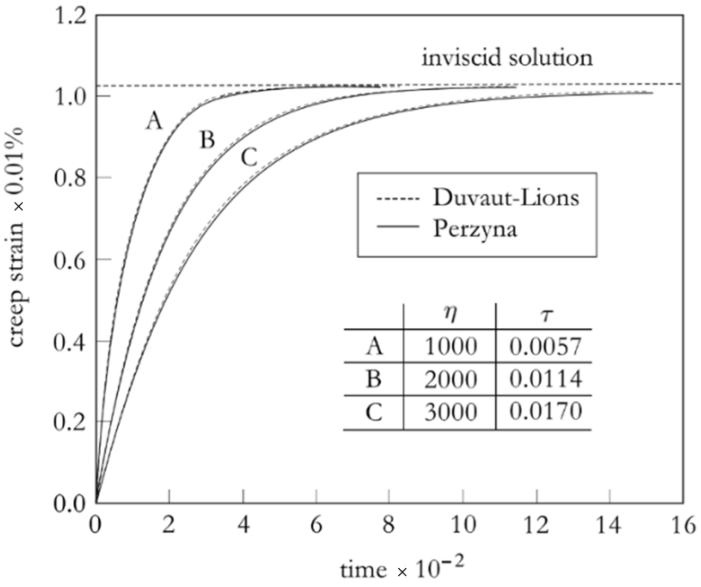

	η	τ
A	1000	0.0057
B	2000	0.0114
C	3000	0.0170

Figure 1. Comparison of axial creep strain with time—two viscoplastic models. Units: η is in $MPa^3 \cdot h$; τ and time are in hours [12].

However, the effect of reservoir creep is rarely considered in fracture conductivity modeling. Meanwhile, several scholars have applied viscoelastic models to account for the creep embedments [17–20]. For example, [19] introduced the modified Burgers creep model into the discontinuous embedment model for multiple-particle-size proppants. They combined it with the KC equation to develop a conductivity prediction model. The results

show that with an increase in rock viscosity, the fracture conductivity decreased to the same level at approximately 300 days. Ref. [18] applied the Burgers model to investigate the role of shale creep on proppant embedment and fracture conductivity. Ref. [17] utilized the fractional Maxwell model to characterize the viscoelastic deformation of tight sandstones. Combining the fractional Maxwell model with Hertz contact theory, an analytical model of fracture width was established. Therefore, based on the classical Perzyna viscoplastic model, the elasto-viscoplastic constitutive model is obtained by introducing isotropic hardening. The constitutive model is programmed in a software platform using the return mapping algorithm, and the model is verified. Then, the elasto-viscoplastic constitutive model is applied to the simulation of the long-term conductivity of the fracture to study the influence of creep on the fracture width.

2. Constitutive Formulation

2.1. Elastic–Viscoplastic Constitutive Formulation

The bedding planes and the fractures within them are the main sources of creep anisotropy [10], and the results of many shale creep experiments show that the strain of shale in the horizontal bedding sample is larger than that in the vertical bedding sample [4,21]. Shale comprises hard materials (quartz, feldspar, and pyrite) and soft materials (clay, kerogen, etc.). The creep is mainly caused by clay and organics. Ref. [22] conducted nanoindentation tests on hard frames (quartz and pyrite), clay, and kerogen in shale. Experimental results showed that the hard frame exhibited anisotropic responses, whereas the responses of clay and kerogen were isotropic [23–25]. Therefore, we assume that the creep behavior of shale is isotropic, and that the anisotropy of shale is mainly reflected in elastic deformation. Since we focus on the creep properties of shale, the anisotropy of shale elasticity is not considered, and a linear elastic constitutive formulation is adopted.

We assumed that the total strain ε_{ij} can be decomposed into elastic strain ε_{ij}^{e} and viscoplastic strain ε_{ij}^{vp}

$$\varepsilon_{ij} = \varepsilon_{ij}^{e} + \varepsilon_{ij}^{vp} \tag{1}$$

The linear elastic constitutive equation is as follows [26]:

$$\sigma_{ij} = C_{ijkl}\varepsilon_{kl}^{e} \tag{2}$$

where σ_{ij} is the stress tensor, and C_{ijkl} is the fourth-order elasticity tensor. C_{ijkl} can be expressed as

$$C_{ijkl} = \lambda\delta_{ij}\delta_{kl} + 2\mu\delta_{ik}\delta_{jl} \tag{3}$$

where λ and μ are Lame constants, which can be expressed by the elastic modulus E and Poisson's ratio ν. δ_{ij}, δ_{kl}, δ_{ik}, and δ_{jl} are Kronicker symbols.

According to the Perzyna-type viscoplastic model [27–29], the viscoplastic strain rate $\dot{\varepsilon}_{ij}^{vp}$ can be expressed as

$$\dot{\varepsilon}_{ij}^{vp} = \dot{p}\frac{\partial g}{\partial \sigma_{ij}} \qquad \dot{p} = \frac{\langle f \rangle}{\eta} \tag{4}$$

where $\dot{p}$ is the viscoplastic multiplier, which determines the magnitude of the viscoplastic strain rate, and the unit is s^{-1}. $\frac{\partial g}{\partial \sigma_{ij}}$ determines the direction of the viscoplastic strain rate. η is the viscosity constant, and the unit is MPa·s. f and g are the yield function and plastic potential function, respectively. The associated viscoplastic flow rule is adopted, Therefore, f equals g. $\langle f \rangle$ is defined as follows:

$$\langle f \rangle = \begin{cases} 0, f \leq 0 \\ f, f > 0 \end{cases} \tag{5}$$

The von Mises yield function considering isotropic hardening can be expressed as follows:

$$f = \sigma_e - \sigma_{y0} - hp \tag{6}$$

where $\sigma_e (\sigma_e = \sqrt{\frac{3s_{ij}s_{ij}}{2}})$ is the von Mises equivalent stress, $\boldsymbol{s_{ij}} (\boldsymbol{s_{ij}} = \boldsymbol{\sigma_{ij}} - \frac{\sigma_{kk}}{3}\boldsymbol{\delta_{ij}})$ is the stress deviator tensor, σ_{y0} is the initial yield stress, and h is the hardening material parameter. σ_{y0} determines the size of the initial yield surface.

When the von Mises equivalent stress is less than or equal to the initial yield stress ($\sigma_e \leq \sigma_{y0}$, $f \leq 0$), the viscoplastic strain rate $\dot{p}$ is 0, and accordingly, the viscoplastic strain p is also 0. When the von Mises equivalent stress is greater than the initial yield stress ($\sigma_e > \sigma_{y0}$, $f > 0$), viscoplastic strain rate $\dot{p}$ is generated, and viscoplastic strain p accumulates accordingly (the yield surface expands due to isotropic hardening). The magnitude of the viscoplastic strain rate is $\frac{f}{\eta}$, substituting (6) into

$$\dot{p} = \frac{f}{\eta} = \frac{\sigma_e - hp - \sigma_{y0}}{\eta} \tag{7}$$

By solving this differential Equation (7), the viscoplastic strain p can be written as

$$p = Ce^{-\frac{h}{\eta}t} + \frac{\sigma_e - \sigma_{y0}}{h} \tag{8}$$

When $t = 0$, the viscoplastic strain p is p_0.

$$p = C + \frac{\sigma_e - \sigma_{y0}}{h} = p_0 \tag{9}$$

It can be seen that C can be obtained from Equation (9). Therefore, C is not an independent material constant but depends on von Mises equivalent stress σ_e, the hardening material parameter h, and the initial yield stress σ_{y0}.

When $t \to \infty$, the viscoplastic strain p tends to a fixed value. Figure 2 shows a schematic of the elastic–viscoplastic model.

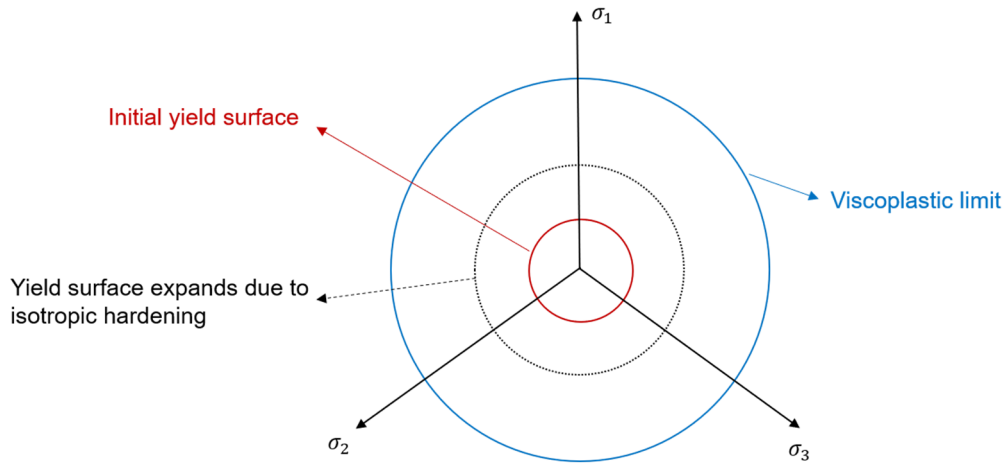

Figure 2. Schematic illustration of elastic–viscoplastic model.

2.2. Power Law Model

The power law model is introduced here only for comparison creep calculation results with the elastic–viscoplastic model.

The creep strain rate of the power law model of time hardening form can be expressed in Equation (10):

$$\dot{\varepsilon} = A\sigma_e^m t^n \tag{10}$$

where σ_e^{m} is the von Mises equivalent stress, and t is the time. A, m, and n are material constants. A and m must be positive and $-1 < n \leq 0$.

3. Modeling Creep in Shale

3.1. Triaxial Creep Experiment

The shale samples used in the experiment come from the Chang 7 reservoir in Ordos Basin, with a depth of about 3000–4000 m. We conducted three creep experiments on three cylindrical samples with a diameter of 25 mm and a height of 50 mm in a servo-controlled triaxial apparatus at a temperature of 110 °C. The specimen wrapped in the heat-shrink jacket was placed in the confining cell. Hydrostatic confining pressure was applied to the specimen to 5 MPa and then held constant. Next, the axial differential stress was increased to a fixed value and kept constant for 8 h. Figure 3 shows the axial strain data of three shale samples under a confining pressure of 5 MPa and differential stresses of 10 MPa, 15 MPa, and 20 MPa.

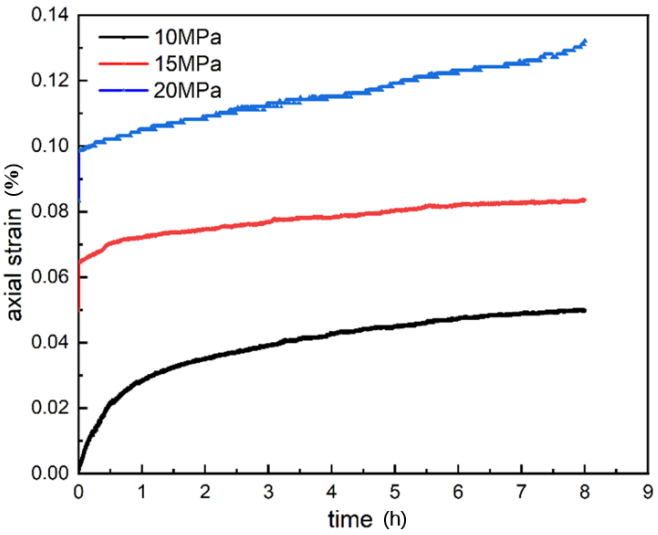

Figure 3. Axial strain data when the differential stress is 10MPa, 15 MPa, and 20 MPa.

The core samples do not enter the tertiary creep stage when differential stress is 10 MPa or 15 MPa, and only show primary and secondary creep, in which the creep strain rate decreases with time and remains constant. When differential stress is 20 MPa, the shale sample exhibits all three stages of creep. A comparison of axial strain data under different differential stresses shows that the shale sample enters the steady-state creep phase faster with increase in differential stress. For example, when the differential stress is 15 MPa, the time from primary creep to steady-state creep is about half that when the differential stress is 10 MPa. When the differential stress is 20 MPa, the time from primary creep to steady-state creep is shortened, and primary creep is hardly observed.

3.2. Parameter Identification

The elastic parameters in the elastic–viscoplastic constitutive model are calculated as follows. We take the ratio of stress to strain of the elastic stage of the axial strain data as the elastic modulus E, and Poisson's ratio ν is assumed to be 0.3. Equation (8) is used to fit the creep strain experimental data to obtain viscoplastic model parameters. Uniaxial or triaxial compression tests must be performed to determine the initial yield stress σ_{y0}, and 1 MPa is assumed here. The fitting results are shown in Figure 4.

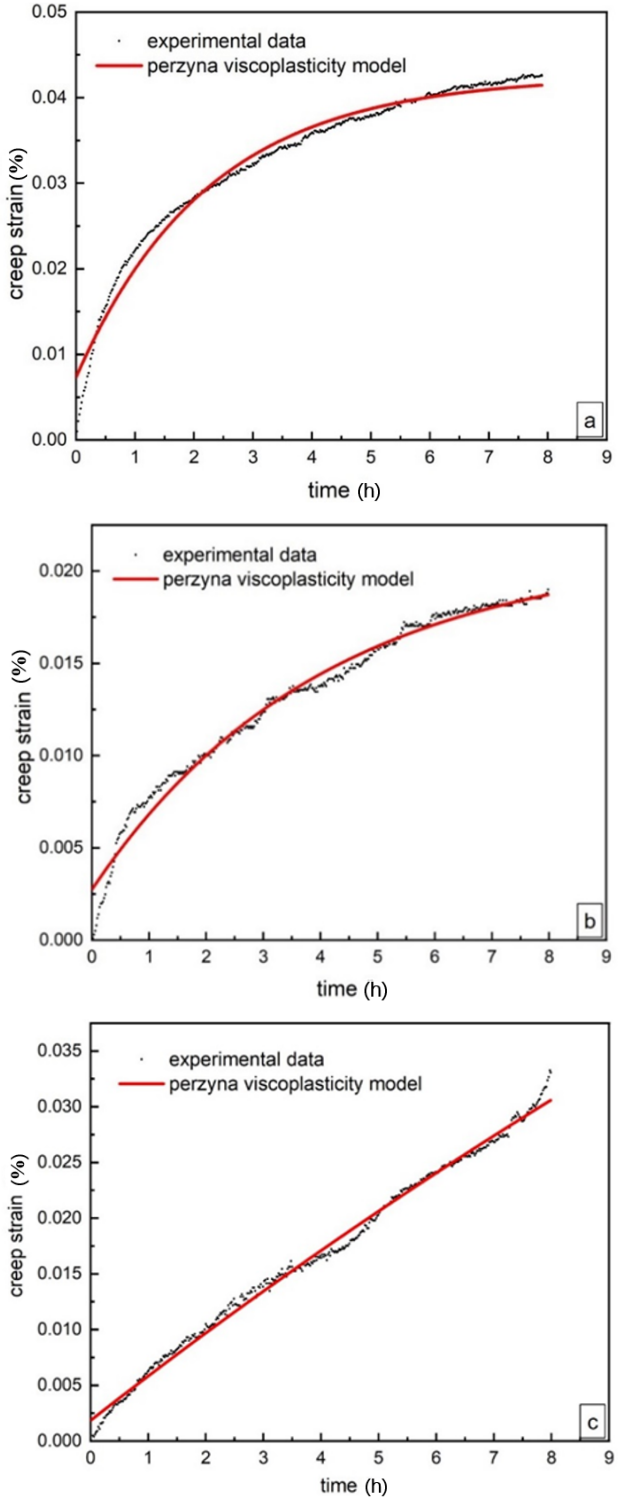

Figure 4. Viscoplastic model fitting experimental data: (**a**) differential stress is 10 MPa; (**b**) differential stress is 15 MPa; (**c**) differential stress is 20 MPa.

Table 1 lists the viscoplastic model parameters obtained by fitting experimental data.

Table 1. Material parameters obtained by fitting.

Differential Stress (MPa)	C	η (MPa·h)	h (MPa)
10	-3.51×10^{-4}	47,598.67	21,174.86
15	-1.85×10^{-4}	264,287.20	65,884.27
20	−0.00137	464,192	13,708

3.3. Algorithm Implementation

The elastic–viscoplastic constitutive model is programmed into the software platform using the return mapping algorithm [30]. The algorithm is divided into two steps: the first step is elastic prediction, and the second step is inelastic correction [26].

Elastic prediction refers to the update of stress calculated according to Equation (11). The stress obtained at this point is called the probing stress $\boldsymbol{\sigma_{ij}}^{\boldsymbol{tr}}$.

$$\boldsymbol{\sigma_{ij}}^{\boldsymbol{tr}} = \boldsymbol{\sigma_{ij}}^{\boldsymbol{n}} + \Delta\sigma = \boldsymbol{\sigma_{ij}}^{\boldsymbol{n}} + \boldsymbol{C_{ijkl}} : \Delta\varepsilon \tag{11}$$

In the formula, $\Delta\sigma$ is the stress increment, $\boldsymbol{C_{ijkl}}$ represents the fourth-order elastic tensor, and $\Delta\varepsilon$ is the strain increment. We set the magnitude of the viscoplastic strain p as the state variable and keep it constant at this step, i.e., $p^{n+1} = p^n$, with the initial $p = 0$.

We can substitute Equation (11) into the expression of the yield function to obtain Equation (12) and check if it is greater than 0.

$$f(\boldsymbol{\sigma_{ij}}^{\boldsymbol{tr}}) = \sigma_e{}^{tr} - \sigma_{y0} - hp^{n+1} \tag{12}$$

In the formula, $\sigma_e{}^{tr}$ is the von Mises equivalent stress calculated from $\boldsymbol{\sigma_{ij}}^{\boldsymbol{tr}}$. If the yield function $f \leq 0$ is used, the material exhibits elasticity, and the stress tensor $\boldsymbol{\sigma_{ij}}^{\boldsymbol{n+1}}$ in step $n + 1$ is the probing stress.

If the yield function $f > 0$, the material has entered the viscoplastic stage; subsequently, it enters the second step of inelastic correction. The stress derivation for step $n + 1$ is as follows:

$$\boldsymbol{\sigma_{ij}}^{\boldsymbol{n+1}} = \boldsymbol{\sigma_{ij}}^{\boldsymbol{n}} + \Delta\sigma = \boldsymbol{\sigma_{ij}}^{\boldsymbol{n}} + \boldsymbol{C_{ijkl}} : (\Delta\varepsilon - \Delta\varepsilon_{vp}) = \boldsymbol{\sigma_{ij}}^{\boldsymbol{n}} + \boldsymbol{C_{ijkl}} : \Delta\varepsilon - \boldsymbol{C_{ijkl}} : \Delta\varepsilon_{vp} \tag{13}$$

In the formula, $\Delta\varepsilon_{vp}$ is the increment in viscoplastic strain. Substituting Equation (11) into Equation (13) yields

$$\boldsymbol{\sigma_{ij}}^{\boldsymbol{n+1}} = \boldsymbol{\sigma_{ij}}^{\boldsymbol{tr}} - \boldsymbol{C_{ijkl}} : \Delta\varepsilon_{vp} \tag{14}$$

Substituting the expression $\Delta\varepsilon_{vp}$ into Equation (14) yields

$$\boldsymbol{\sigma_{ij}}^{n+1} = \boldsymbol{\sigma_{ij}}^{\boldsymbol{tr}} - \boldsymbol{C_{ijkl}} : \dot{p}\frac{\partial f}{\partial \boldsymbol{\sigma_{ij}}}\Delta t \tag{15}$$

In the formula, Δt is the time increment. Substituting $\frac{\partial f}{\partial \sigma_{ij}} = \frac{3s_{ij}{}^{tr}}{2\sigma_e{}^{tr}}$ into Equation (15) yields

$$\boldsymbol{\sigma_{ij}}^{n+1} = \boldsymbol{\sigma_{ij}}^{\boldsymbol{tr}} - \boldsymbol{C_{ijkl}} : \dot{p}\frac{3\boldsymbol{s_{ij}}^{\boldsymbol{tr}}}{2\sigma_e{}^{tr}}\Delta t \tag{16}$$

Considering $\boldsymbol{C_{ijkl}} : \boldsymbol{s_{ij}}^{\boldsymbol{tr}} = 2G\boldsymbol{s_{ij}}^{\boldsymbol{tr}} + \lambda \boldsymbol{s_{ii}}\boldsymbol{\delta_{ij}} = 2G\boldsymbol{s_{ij}}^{\boldsymbol{tr}}$, substituting it into Equation (16) yields

$$\boldsymbol{\sigma_{ij}}^{n+1} = \boldsymbol{\sigma_{ij}}^{\boldsymbol{tr}} - 2G\dot{p}\frac{3\boldsymbol{s_{ij}}^{\boldsymbol{tr}}}{2\sigma_e{}^{tr}}\Delta t \tag{17}$$

According to Equation (17), the stress $\boldsymbol{\sigma_{ij}}^{\boldsymbol{n+1}}$ at step $n + 1$ depends on the value of $\dot{p}$. The following solution process of $\dot{p}$ is provided.

We can satisfy the equation $\dot{p} = \frac{f}{\eta}$; for ease of calculation, we can rewrite it as $\Delta p = \dot{p}\Delta t = \frac{f}{\eta}\Delta t$ and solve it through Newton's iteration. The specific derivation process is as follows:

$$\Delta p - \frac{f}{\eta}\Delta t + (1 - \frac{f'_{\Delta p}}{\eta}\Delta t)d\Delta p = 0 \tag{18}$$

In the formula, $f'_{\Delta p}$ is the derivative of the yield function f to Δp. Substituting the expression of the yield function into Equation (18) yields the following:

$$\Delta p - \frac{{\sigma_e}^{n+1} - \sigma_{y0} - hp^{n+1}}{\eta}\Delta t + (1 - \frac{\partial({\sigma_e}^{n+1} - \sigma_{y0} - hp^{n+1})}{\partial \Delta p}\frac{\Delta t}{\eta})d\Delta p = 0 \tag{19}$$

Considering that $\boldsymbol{\sigma_e}^{\boldsymbol{n+1}} = {\sigma_e}^{tr} - 3G\Delta p$, substituting it into Equation (19) yields the following:

$$\Delta p - \frac{{\sigma_e}^{n+1} - \sigma_{y0} - hp^{n+1}}{\eta}\Delta t + (1 - \frac{\partial({\sigma_e}^{tr} - 3G\Delta p - \sigma_{y0} - hp^{n+1})}{\partial \Delta p}\frac{\Delta t}{\eta})d\Delta p = 0 \tag{20}$$

Solution:

$$(\Delta p)^{n+1} = (\Delta p)^n + \frac{\frac{f}{\eta}\Delta t - (\Delta p)^n}{1 + (3G + h)\frac{\Delta t}{\eta}} \tag{21}$$

The increment in viscoplastic strain is calculated based on Δp, i.e.,

$$\Delta \varepsilon_{vp} = \Delta p \frac{\partial f}{\partial \boldsymbol{\sigma_{ij}}} \tag{22}$$

The increment in elastic strain is

$$\Delta \varepsilon_e = \Delta \varepsilon - \Delta \varepsilon_{vp} \tag{23}$$

The stress at step $n + 1$ is

$$\boldsymbol{\sigma_{ij}}^{\boldsymbol{n+1}} = \boldsymbol{\sigma_{ij}}^{\boldsymbol{n}} + \Delta\sigma = \boldsymbol{\sigma_{ij}}^{\boldsymbol{n}} + \boldsymbol{C_{ijkl}} : \Delta\varepsilon_e \tag{24}$$

The initial elastic stiffness matrix is still used here. The flowchart of the entire algorithm is shown in Figure 5.

3.4. Elastic–Viscoplastic Model Validation

In this study, we simulate numerical creep experiments under triaxial loading to verify the correctness of the viscoplastic constitutive relationship. Using the axisymmetric model shown in Figure 6, the leftmost dashed line in the figure represents the axis of symmetry. In order to compare with the experimental data, the geometric dimensions, loads, and boundary conditions were set the same as those of the shale sample creep experiment. The elastic parameters are taken as Young's modulus E = 25 GPa and Poisson's ratio ν = 0.3. The parameters of the viscoplastic material are determined by fitting the viscoplastic constitutive model to the first set of experimental data and the third set of experimental data.

In order to improve the accuracy of the calculation, the unit type used is CAX4. We use structured grid partitioning technology to divide the model into 1000 units. We set two static analysis steps. In the first analysis step, confining pressure and axial pressure are applied, and the load increases linearly with time, with a loading time of 90 s. In the second analysis step, the load remains unchanged, with a total time of 7.995 h. In order to obtain the same number of data points as the experiment, a fixed step size of 10 s is used.

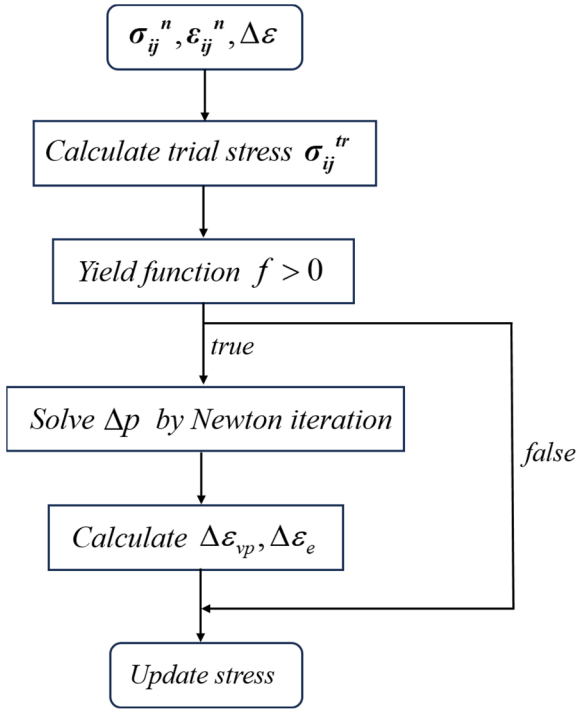

Figure 5. Return mapping algorithm for elasto-viscoplastic constitutive model.

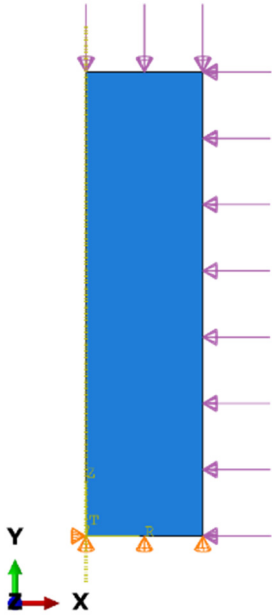

Figure 6. Numerical creep experimental model under triaxial compression (The arrow represents pressure loading and the triangle represents support).

Figure 7 shows a comparison between simulation results and experimental data.

As shown in Figure 7a, during the decay creep stage, there is a gap between the numerical calculation results of the viscoplastic model and the experimental data. After entering the steady-state creep stage (about 3 h), the simulation results agree with the experimental data. As shown in Figure 7b, the numerical calculation results of the viscoplastic model are in good agreement with the experimental data.

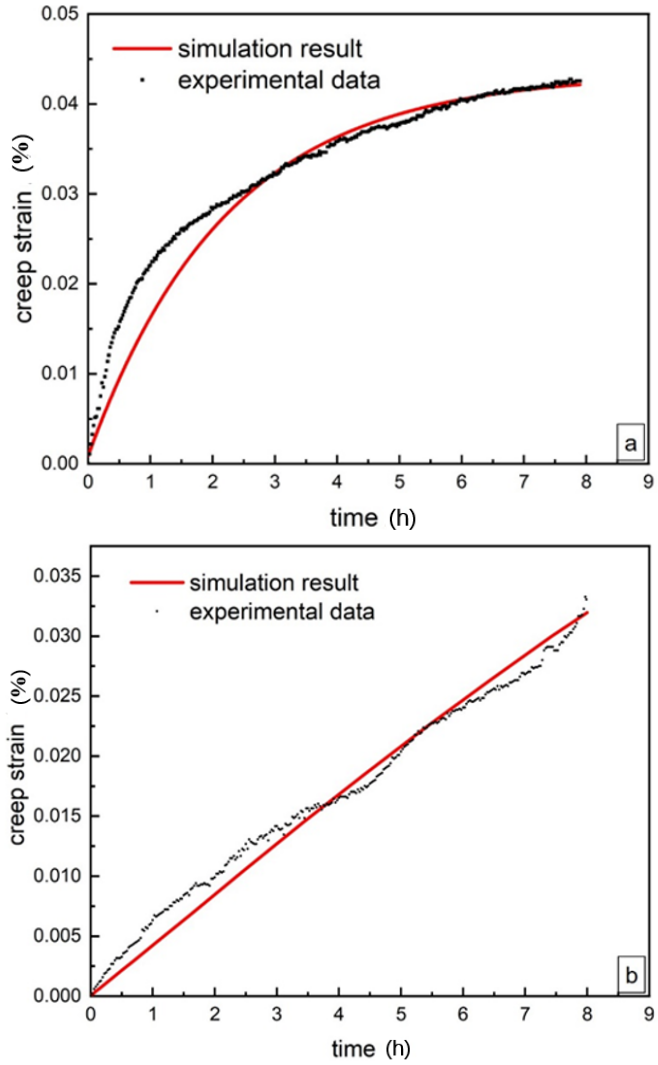

Figure 7. Comparison between simulation results and experimental data. (**a**) differential stress is 10 MPa; (**b**) differential stress is 20 MPa.

There may be two possible reasons for the discrepancy between the numerical calculation results of the viscoplastic model during the attenuation creep stage in Figure 7a and the experimental data. The first is the influence of shale anisotropy: compared to sandstone, shale exhibits significant anisotropy due to bedding planes. The viscoplastic model itself is an ideal model that does not consider the presence of internal pores, fractures, and defects in the rock core. However, there are many natural original fractures within the actual shale core itself. These original fractures may close in the early stage of creep, and over time, they may expand and even cause creep fractures (Wang, 2012) [31]. Therefore, the rate of decay creep is relatively high in the early creep stage.

Figure 8 compares the simulation results of the viscoplastic model and the power law model inherent in the software platform and the third set of experimental data. As shown in the figure, both the viscoplastic model and the power law model are in good agreement with the creep experimental results.

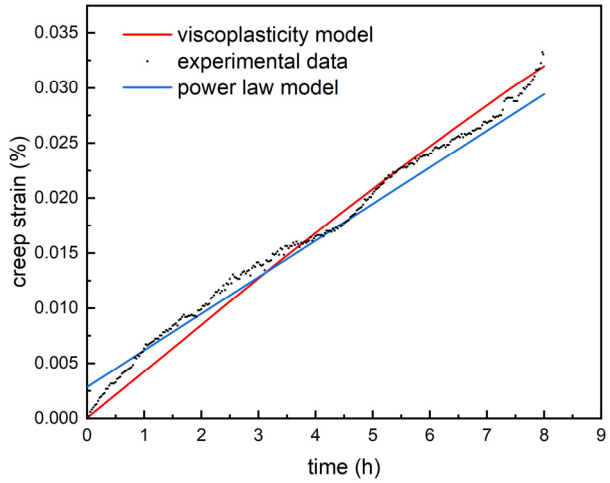

Figure 8. Comparison of simulation results of viscoplastic model and power law model with experimental data.

3.5. Parameter Analysis of Elastic–Viscoplastic Model

This section conducts sensitivity analysis on the viscosity parameters, initial yield stress, and strengthening material parameters in the elasto-viscoplastic constitutive model to understand their impact on creep strain.

Figure 9 shows the variation curve of creep strain over time under different viscosity parameters. Figure 10 shows the time-dependent curves of creep strain at initial yield stresses of 0.3 MPa, 0.8 MPa, and 1.3 MPa. Figure 11 shows the time-dependent creep strain curves of reinforced materials with parameters of 11,210.76 MPa, 21,210.76 MPa, and 31,210.76 MPa.

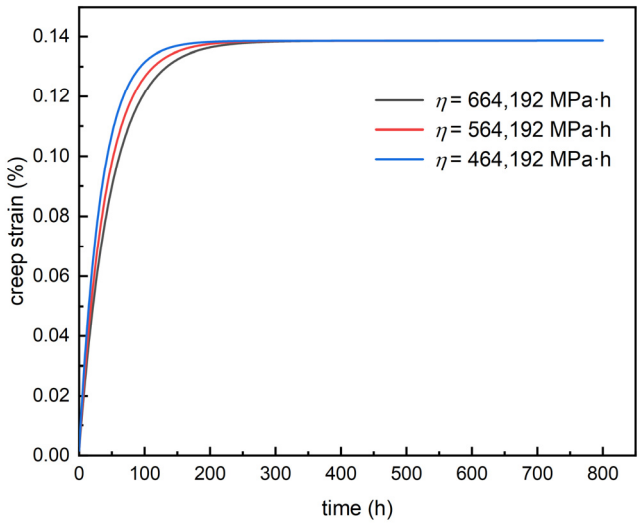

Figure 9. Influence of different viscous parameters on creep curve.

In Figure 9, under certain other conditions, as the viscosity parameter increases, the creep strain rate decreases, and the time to reach the "limit" of creep strain extends. That is, the viscosity parameter only affects the time to reach the maximum creep strain and does not affect the final creep strain. When the viscosity parameter is set, the creep strain limit is closer to the initial yield surface—that is, the viscoplastic solution is closer to the "pure" plastic solution [29]. As shown in Figure 10, under certain other conditions, the larger the initial yield stress, the smaller the creep strain rate and creep strain. For every 0.5 MPa increase in initial stress, the creep strain decreases by approximately 0.23×10^{-4}. As shown in Figure 11, under certain other conditions, as the strengthening material parameters

increase, the creep strain decreases. Furthermore, there is a non-linear relationship between creep strain and strengthening material parameters.

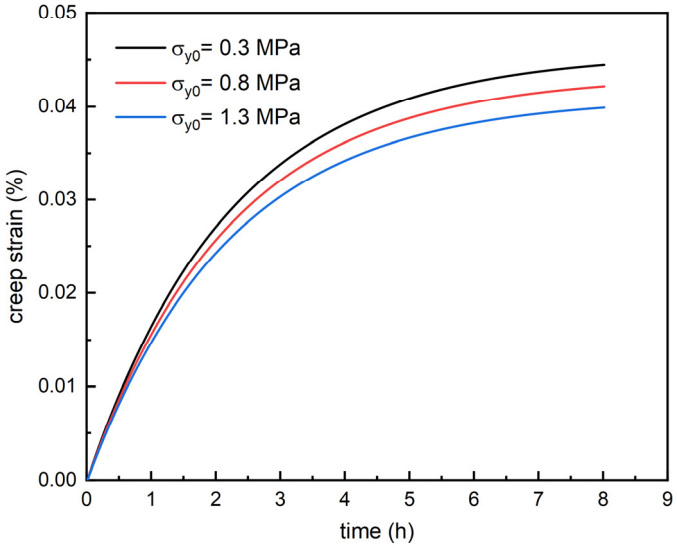

Figure 10. Effect of initial yield stress on creep strain.

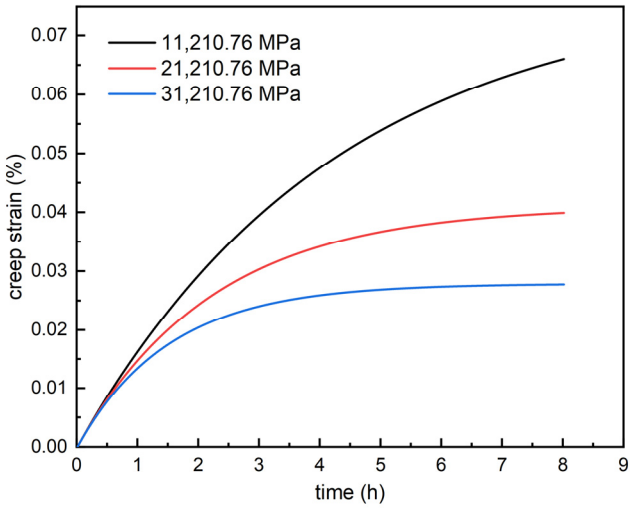

Figure 11. Creep strain versus time for different strengthening material parameters.

4. Fracture Conductivity Simulation

We use finite element analysis software to apply the elasto-viscoplastic constitutive model to the analysis of fracture conductivity, study the influence of creep on fracture width, and analyze the factors influencing fracture width.

4.1. Fracture Conductivity Model Setup

We can simplify the plane strain problem of the rock fracture system and adopt the following assumptions in modeling:

1. We do not consider the poro-elastic characteristics of shale;
2. The permeability of the fracture remains constant; it does not take into account the changes in fracture permeability caused by the decrease in pore pressure, the increase in effective stress on the proppant, and the detachment of the reservoir caused by the embedding of the proppant, leading to the migration of debris and proppant;
3. There is an intermediate layer in the middle of the fracture, in addition to the relatively large size of the proppant, which is believed to be composed of relatively small

proppant particles, pores, and rock debris, and crystallization and clay-like minerals formed by pressure solution diagenesis in the proppant [20];

4. We can ignore the influence of proppant gravity and fracture surface roughness.

Figure 12 shows the geometric model of the rock fracture system. Shale reservoirs are located above and below, with proppant-filled layers between the reservoirs. The circular particles in the middle are relatively larger proppant particles (double-layer proppant is used here). The intermediate layer is in contact with the relatively larger proppants of the upper and lower reservoirs (the following proppants refer to larger proppants). The reservoir is 1.5 cm thick, with a fracture length of 5 cm, a width of 2 cm, and a proppant radius of 5 mm. Except for the CPE4P element, which is a seepage displacement coupling element with pore pressure degrees of freedom, all other components use the CPE4 element.

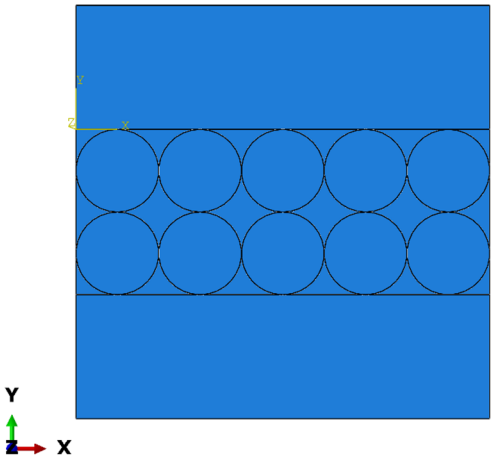

Figure 12. Geometry model of rock fracture system.

The material parameters are shown in Table 2.

Table 2. Material parameters.

Model Material Parameter	Specific Value
Elastic modulus of proppant (GPa)	30
Proppant Poisson's ratio	0.3
Elastic modulus of shale reservoirs (GPa)	20
Poisson's ratio of shale	0.25
Initial yield strength (MPa)	1
Strengthening material parameters (MPa)	14,276.18
Viscosity parameter (MPa·h)	461,543.53
Elastic modulus of intermediate layer (MPa)	100
Intermediate Poisson's ratio	0.3
Liquid gravity (kN/m^3)	10
Permeability coefficient (m/s)	10^{-10}
Fluid bulk modulus (GPa)	2

Figure 13 shows the setting of boundary conditions for the model. We can fix the horizontal and vertical displacement of the bottom surface. The horizontal displacement of all components is limited, and only a vertical pressure of 85 MPa is applied on the top surface. Considering that the pore fluid in the middle layer flows toward the wellbore under closed pressure, we set the right boundary of the middle layer to have a pore pressure of 0. The initial porosity ratio of the intermediate layer is set to 0.67. The decrease in pore fluid pressure causes an increase in the effective stress on the proppant, and the compaction process of the proppant is achieved through the contact between the larger proppant and the upper and lower reservoirs, as well as between the intermediate layer and the upper and lower reservoirs.

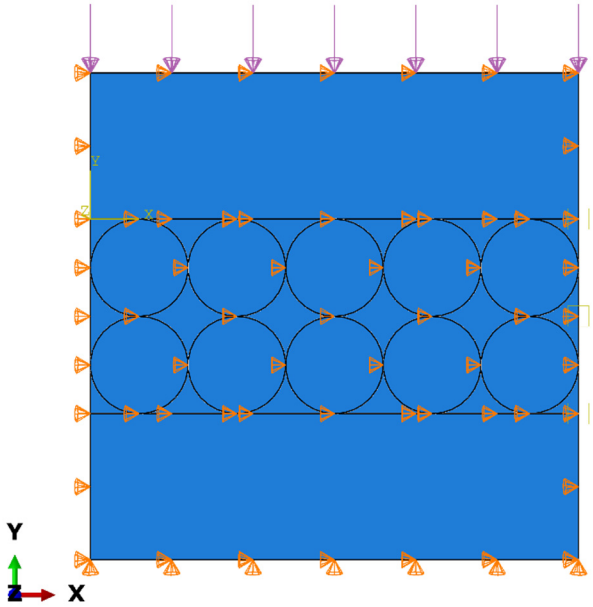

Figure 13. Load and boundary condition settings (The arrow represents pressure loading and the triangle represents support).

The specific settings for contact are as follows. Each proppant is set as the contact surface, the upper and lower surfaces of the reservoir are set as the contact surface, the upper and lower surfaces of the intermediate layer are set as the contact surface, and the entire intermediate layer is set as the contact surface. A contact pair is set between each proppant in the first layer and the lower surface of the reservoir. Usually, the surface with high stiffness is chosen as the main surface, so the proppant is the main surface, and the lower surface of the reservoir is the secondary surface. A contact pair is set between each proppant in the second layer and the upper surface of the reservoir, with the proppant as the main surface and the upper surface of the reservoir as the secondary surface. A contact pair is set between the upper surface of the intermediate layer and the lower surface of the reservoir, with the lower surface of the reservoir being the main surface and the upper surface of the intermediate layer being the secondary surface. A contact pair is set between the lower surface of the intermediate layer and the upper surface of the reservoir, with the upper surface of the reservoir being the main surface and the lower surface of the intermediate layer being the secondary surface. The contact properties are set to normal hard contact, and the penalty friction formula with a friction coefficient of 0.5 is used for tangential contact. We can set binding constraints between the entire intermediate layer and each proppant, with the proppant as the main surface and the intermediate layer as the secondary surface.

4.2. Results

Figures 14 and 15, respectively, show the overall stress distribution cloud maps of the model at 0.3 h and 72 h, as well as the stress distribution cloud maps of the support agent. Figure 16 shows the overall vertical displacement cloud maps of the model at 0.3 h and 72 h.

Based on Figures 14 and 15, it can be seen that the von Mises stress in the contact area between the upper and lower layers of the proppant is the highest, with a maximum von Mises stress of 1151.19 MPa. The von Mises stress in the contact area between the proppant and the upper and lower reservoir rocks is secondary, with a maximum von Mises stress of 854.54 MPa. This is mainly because the elastic moduli of the upper and lower layers of proppants are equal, and they are less prone to deformation when in contact. The elastic modulus of the proppant is slightly higher than that of shale, and the contact between the two is relatively prone to deformation. Moreover, as the closing pressure increases and time passes, the proppant is more likely to be embedded into shale reservoirs.

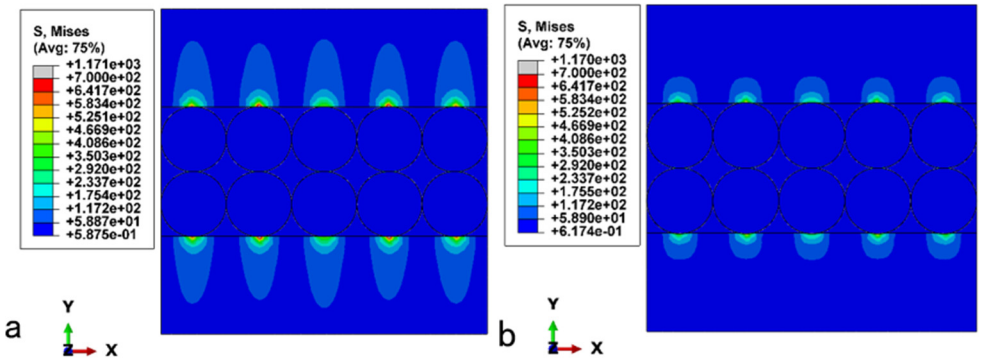

Figure 14. von Mises stress of conductivity model (**a**) at 0.3 h; (**b**) at 72 h. (The scientific notation e+03 means $\times 10^3$).

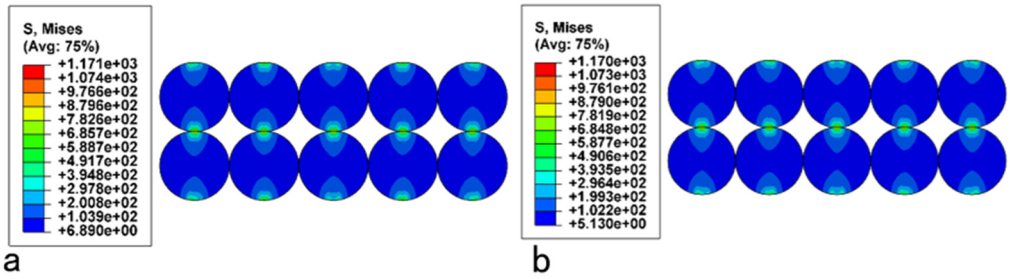

Figure 15. von Mises stress of proppants (**a**) at 0.3 h; (**b**) at 72 h. (The scientific notation e+03 means $\times 10^3$).

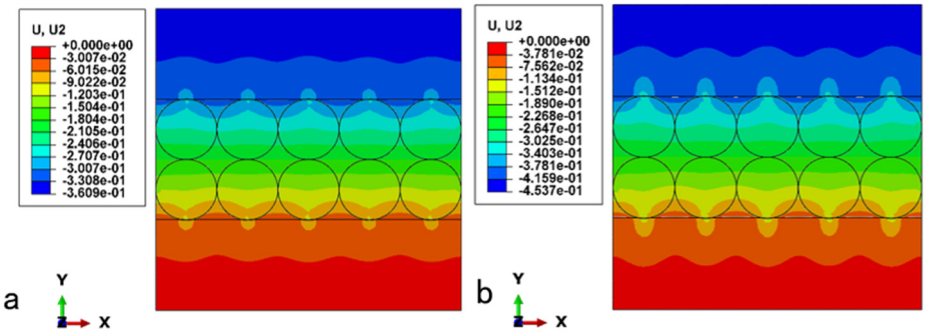

Figure 16. Vertical displacement of conductivity model (**a**) at 0.3 h; (**b**) at 72 h. (The scientific notation e+03 means $\times 10^3$).

Comparing the overall von Mises stress cloud maps of the 0.3 h and 72 h models with the von Mises stress cloud maps of the proppant, it is easy to find that the von Mises stress at 0.3 h is lower than that at 72 h, especially in the contact area between the proppant and the upper and lower shale reservoir rocks, indicating stress relaxation at the fracture surface, which is caused by the dissipation of pore pressure in the intermediate layer.

As shown in Figure 16, the vertical displacement decreases sequentially from the top to the bottom. When the calculation is terminated, the proppant is slightly embedded in the formation, and the amount of proppant embedded in the middle is about 0.0488 mm. The variation in fracture width (referring to the minimum fracture width here) is 0.352 mm. The embedding amount accounts for 27.7% of the half fracture width variation, and the seam width variation rate, which is the ratio of fracture width variation to the original fracture width, is 1.76%.

We defined a path along the exit direction of the fracture surface. Figure 17 shows the distribution pattern of pore pressure in the middle layer along the outlet direction of the fracture surface at different times. Obviously, the pore pressure gradually decreases

along the direction of the fracture surface outlet, reflecting the process of pore pressure dissipation. Figure 18 shows the distribution pattern of flow velocity along the outlet direction of the fracture surface at the end of the calculation. It is easy to see that the flow velocity gradually increases along the direction of the fracture surface outlet, and the flow velocity at the insertion point of the support agent significantly decreases, which indirectly reflects the decrease in permeability in the embedding area and the decrease in diversion capacity.

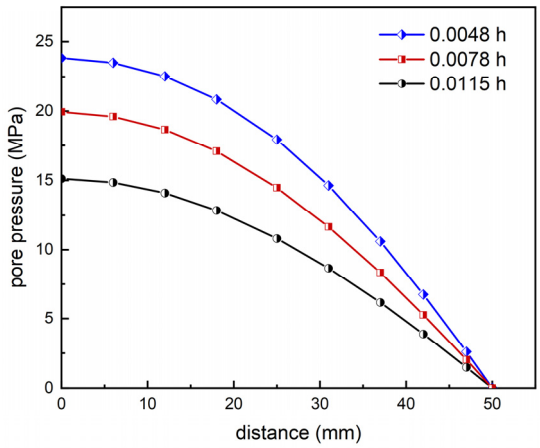

Figure 17. Pore pressure versus distance.

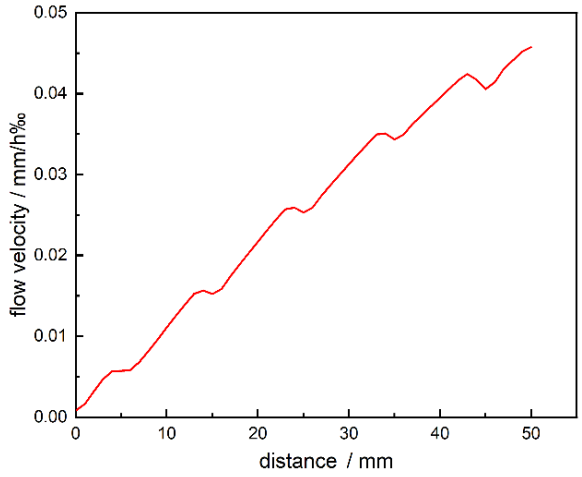

Figure 18. Flow velocity versus distance.

Figure 19 shows the variation in fracture width over time. As shown in the figure, the instantaneous change in fracture width caused by closed stress is about 0.239 mm, accounting for 67.93% of the total fracture width change. Subsequently, the change in fracture width caused by pore pressure dissipation and rock creep accounts for about 32.07%. It can be seen that the changes in fracture width caused by the decrease in pore pressure of the proppant filling layer and the changes in fracture width caused by rock creep cannot be ignored.

4.3. Analysis of Factors Influencing Fracture Width

This section investigates the effects of physical quantities such as the closure pressure, elastic modulus and Poisson's ratio of proppants, the elastic modulus and Poisson's ratio of rocks, viscosity parameters, the strengthening material parameters, and the initial yield stress on the fracture width.

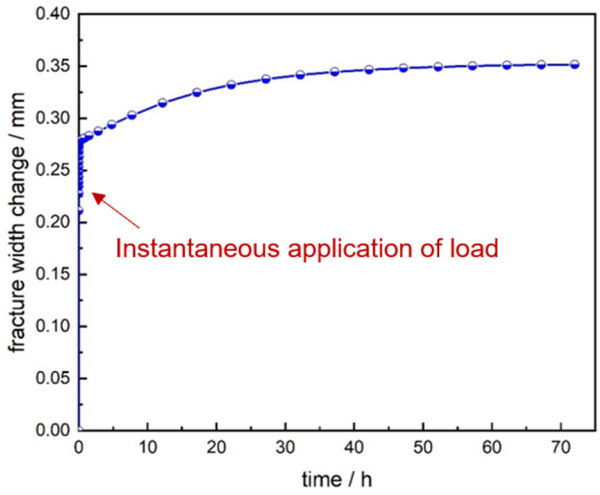

Figure 19. Change in fracture width versus time.

Figure 20 shows the variation in fracture width over time at closure pressures of 45 MPa, 65 MPa, 85 MPa, and 105 MPa. As shown in Figure 20, under certain other conditions, as the closure stress increases, the fracture width gradually decreases. For every 20 MPa increase in closure stress, the fracture width decreases by approximately 0.07 mm. As the closure pressure increases, the time for the fracture width to reach stability is extended. The variation in fracture width can be divided into three stages. At the moment of loading, due to the lack of time for pore pressure to dissipate, the reduction in fracture width is mainly caused by the elastic deformation of the reservoir and proppant. Subsequently, as the pore pressure dissipates, the effective stress on the proppant increases, causing further deformation of the proppant and reservoir, resulting in a decrease in fracture width. After the dissipation of pore pressure, due to the creep properties of the reservoir rock, the reservoir continues to deform, and the fracture width further decreases. As the viscoplastic model of the reservoir is an "upper limit" model, the fracture width will gradually approach a fixed value over time. When the closure stress is increased, it impacts all three stages.

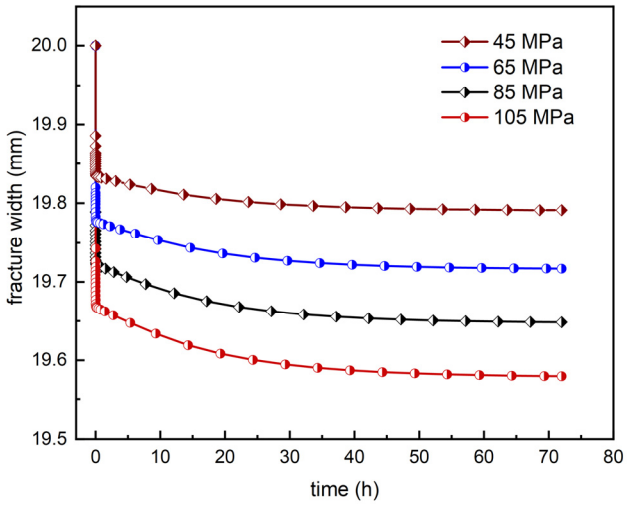

Figure 20. Fracture width versus time for different closing pressures.

Figure 21 shows the variation in fracture width with time when the elastic moduli of the proppant are 30 GPa, 40 GPa, 50 GPa, and 60 GPa. When other conditions are constant, the larger the elastic modulus of the proppant, the wider the fracture width. This is because the larger the elastic modulus of the proppant, the more effectively it can play its role; that is, the proppant is less likely to deform and embed, and fractures are less likely to close.

When the elastic modulus of the proppant increases from 30 GPa to 40 GPa, the decrease in fracture width is greater than when the elastic modulus of the proppant increases from 40 GPa to 50 GPa. This indicates that when the elastic modulus of the proppant increases to a value of around 40 GPa, it can better support fractures. If the elastic modulus of the proppant continues to increase, it cannot significantly reduce the fracture width. When comparing the time-varying curves of the fracture width with different elastic moduli of proppants, the curves are parallel to each other, indicating that the elastic modulus of proppants mainly affects the instantaneous application of closing stress and the early stage of pore pressure dissipation. For the time period after small changes in pore pressure, changes in the elastic modulus of proppants have almost no effect on the fracture width. This is because the change in elastic deformation caused by the change in elastic modulus is not related to the length of time but only to stress.

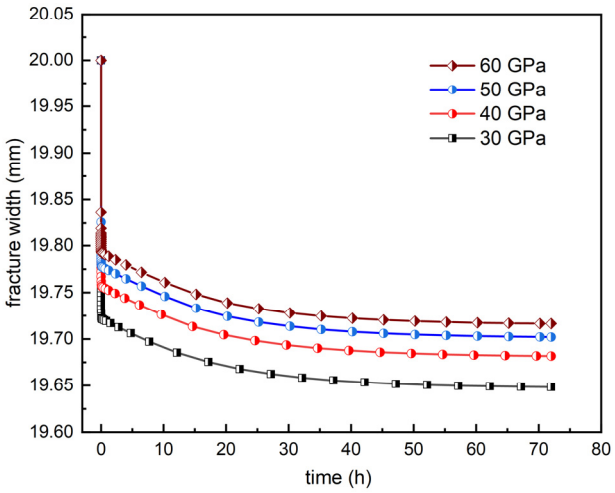

Figure 21. Fracture width versus time for different elastic moduli of proppant.

Figure 22 shows the variation in fracture width with time when the Poisson's ratio of the proppant is taken as 0.2, 0.3, 0.4, and 0.45. As shown in the figure, when other conditions are constant, the larger the Poisson's ratio, the wider the gap. Due to the limitation of all lateral displacements in the diversion capacity evaluation model, deformation can only occur in the vertical direction. The larger the Poisson's ratio of the proppant, the stronger its ability to resist vertical deformation, and the less likely it is to reduce the fracture width. Similarly to Figure 21, the time-dependent curves of fracture width under the influence of different proppant Poisson's ratios are parallel to each other, indicating that the proppant Poisson's ratio mainly affects the instantaneous application of closure stress and the early stage of pore pressure dissipation. For the later stage of pore pressure dissipation, the proppant Poisson's ratio has almost no effect on fracture width. This is because the change in elastic deformation caused by Poisson's ratio is not related to the length of time but only to the change in stress.

Figure 23 shows the variation in fracture width over time for shale reservoirs with elastic moduli of 10 GPa, 15 GPa, 20 GPa, and 30 GPa. As shown in the figure, when other conditions are constant, the larger the elastic modulus of shale reservoirs, the wider the fracture width. The elastic modulus reflects the ability of a reservoir to resist elastic deformation. The larger the elastic modulus, the stronger the resistance to deformation, and the less likely the fracture width is to decrease. The reduction in fracture width caused by the change in elastic modulus from 10 GPa to 20 GPa is 2.61 times that caused by the change in elastic modulus from 20 GPa to 30 GPa. This is because the elastic modulus of the proppant is 30 GPa. As the elastic modulus of the reservoir approaches 30 GPa, the two are evenly matched, making the proppant less likely to deform and the fracture width less likely to decrease. When the elastic modulus of the reservoir and the elastic modulus of the

proppant differ significantly, the proppant is prone to embedding and cannot effectively support the fractures.

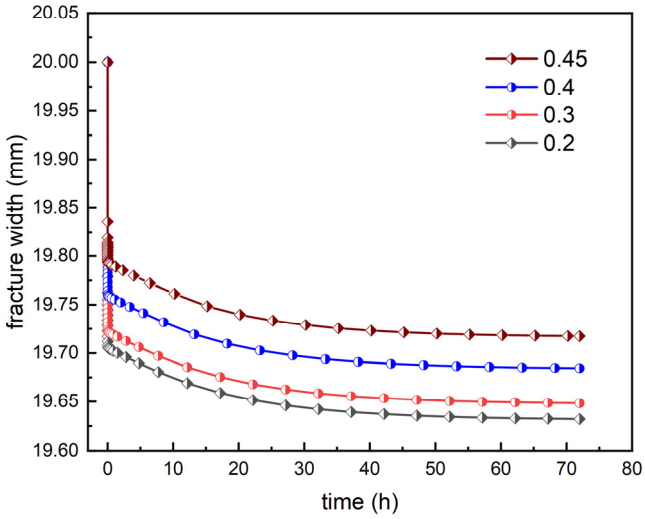

Figure 22. Fracture width versus time for different Poisson's ratios of proppant.

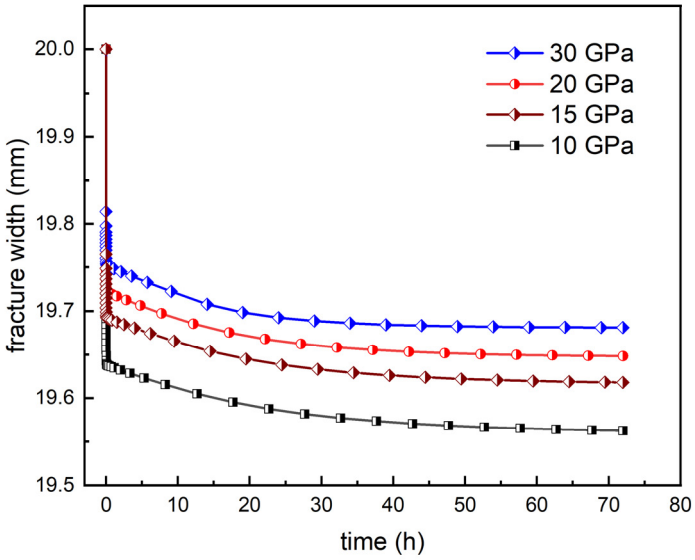

Figure 23. Fracture width versus time for different elastic moduli of reservoir.

Figure 24 shows the variation in fracture width over time for shale reservoirs with Poisson's ratios of 0.2, 0.25, 0.3, and 0.35. As shown in the figure, when other conditions are constant, the larger the Poisson's ratio of the reservoir, the wider the fracture width. The reason for this is the same as the effect of the Poisson's ratio of the proppant on the fracture width, so it will not be repeated here. The width of the fracture is not linearly proportional to the Poisson's ratio of the reservoir. When the reservoir Poisson's ratio increased from 0.2 to 0.25, the fracture width increased by 0.0087 mm; when the reservoir Poisson's ratio increased from 0.25 to 0.3, the fracture width increased by 0.0111 mm; and when the reservoir Poisson's ratio increased from 0.3 to 0.35, the fracture width increased by 0.0144 mm. Similarly to Figure 22, the Poisson's ratio of the reservoir mainly affects the instantaneous application of closure pressure and the early stage of pore pressure dissipation. For the later stage of pore pressure dissipation, the Poisson's ratio of the reservoir has almost no effect on fracture width.

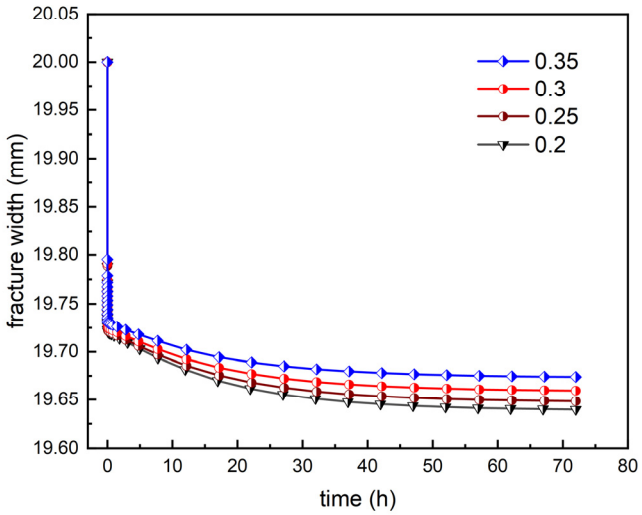

Figure 24. Fracture width versus time for different Poisson's ratios of reservoir.

Figure 25 shows the viscosity parameters of shale reservoirs, which are η = 661,543.53 MPa·h, η = 561,543.53 MPa·h, and η = 461,543.53 MPa·h. The variation law of fracture width with time at 361,543.53 MPa·h. As shown in the figure, for the 72 h diversion capacity evaluation model, changes in viscosity parameters have almost no effect on the final fracture width.

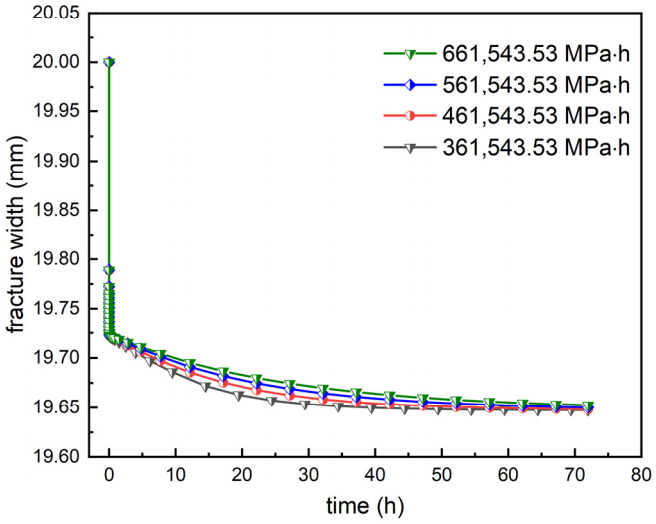

Figure 25. Fracture width versus time for different viscous parameters of reservoir.

Figure 26 shows the variation in fracture width over time at initial yield stresses of 1 MPa, 21 MPa, 41 MPa, and 61 MPa. As shown in the figure, under certain other conditions, as the initial yield stress of the reservoir increases, the fracture width increases. For every 10 MPa increase in initial yield stress, the fracture width increases by approximately 0.01 mm. Although this value is small, it cannot be ignored when measuring the effect of initial yield stress on fracture width on a longer time scale, such as 10 years, given a creep time of 72 h.

Figure 27 shows the variation in fracture width over time when the strengthening material parameters are h = 14,276.18 MPa, h = 24,276.18 MPa, h = 34,276.18 MPa, and h = 44,276.18 MPa. As shown in the figure, when other conditions are constant, as the strengthening material parameters increase, the fracture width increases. The parameters of strengthening materials mainly affect the process of stress, which no longer changes after the dissipation of pore pressure. Increasing the parameters of strengthening materials is equivalent to increasing the subsequent yield stress, resulting in a decrease in creep strain rate, a

decrease in creep strain, and an increase in fracture width. As the variation in pore pressure is small, the variation curves of fracture width with time corresponding to different strengthening materials are not parallel, indicating that the strengthening material parameters are not linearly related to fracture width. This is consistent with the influence of strengthening material parameters on creep strain in Figure 11. Comparing Figures 26 and 27, the influence of strengthening material parameters on seam width is greater than that of initial yield stress on seam width. This is because the initial yield stress is only the "threshold value" for entering viscoplasticity, while the strengthening material parameters affect the entire creep process.

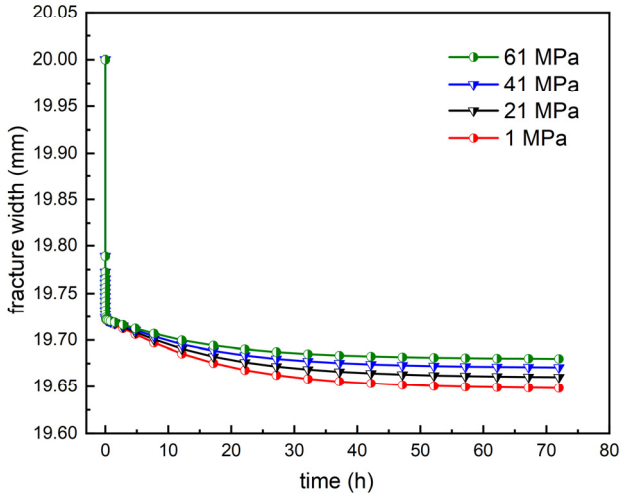

Figure 26. Fracture width versus time for different initial yield stresses of reservoir.

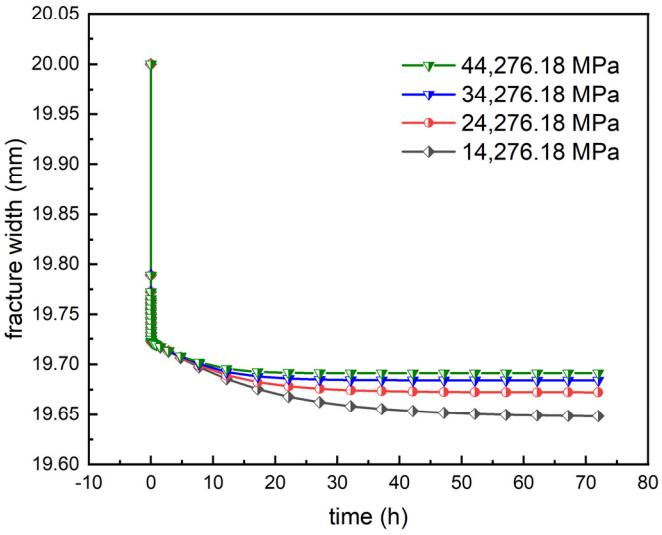

Figure 27. Fracture width versus time for different hardening material parameters of reservoir.

5. Conclusions

This study introduces isotropic strengthening based on the classic Perzyna viscoplastic model to obtain an elastic–viscoplastic constitutive model. The model was used to fit triaxial compression creep experimental data under different differential stresses, obtain model parameters, and program the model in the UMAT subroutine interface for model validation. Finally, the viscoplastic model was applied to the calculation and simulation of long-term fracture conductivity to study the effect of creep on fracture width and to analyze the factors affecting fracture width. The conclusions drawn are as follows:

(1) According to the 8 h high-temperature creep test results of shale with confining pressure of 5 MPa and differential stresses of 10 MPa, 15 MPa, and 20 MPa, shale mainly exhibits characteristics of attenuation creep and steady-state creep.
(2) The verification results of the viscoplastic model indicate that, during the attenuation creep stage at a differential stress of 10 MPa, there is a gap between the numerical calculation results of the viscoplastic model and the experimental data. After entering the steady-state creep stage, the simulation results agree with the experimental data. When the differential stress is 20 MPa, the overall agreement between the viscoplastic model and experimental data is good.
(3) The sensitivity analysis of material parameters in the viscoplastic model shows that the viscosity parameters only affect the time to reach the final creep strain and do not affect the final creep. There is a linear inverse relationship between creep strain and initial yield stress. There is a non-linear inverse relationship between creep strain and strengthening material parameters.
(4) The simulation results of the artificial fracture diversion capacity evaluation model show that, after 72 h, the reduction in fracture width caused by pore pressure dissipation and reservoir creep accounts for 32.07% of the total reduction in fracture width. Further, the viscoplastic deformation of reservoirs cannot be ignored in predicting the hydraulic conductivity of artificial fractures.
(5) The process of fracture width variation can be divided into three stages. The instantaneous application of closed stress, due to the lack of time for pore pressure to dissipate, results in a decrease in fracture width mainly caused by the elastic deformation of the reservoir and proppant. Then, as the pore pressure dissipates, the effective stress on the proppant increases and is transmitted to the reservoir through contact, and the fracture width continues to decrease. When the pore pressure has dissipated and the effective stress on the proppant no longer changes due to the creep properties of the reservoir, the strain will still gradually increase over time until it reaches the maximum value of creep strain, and the fracture width will no longer change.

Author Contributions: Conceptualization, S.L.; Methodology, S.L.; Software, J.Z.; Validation, M.L. (Mengjie Li) and J.L.; Formal analysis, M.L. (Mengjie Li); Investigation, J.L.; Writing—original draft, J.Z.; Writing—review & editing, J.F.; Supervision, S.L.; Project administration, H.G., H.W. and M.L. (Muzi Li); Funding acquisition, H.G., H.W. and M.L. (Muzi Li). All authors have read and agreed to the published version of the manuscript.

Funding: This work was supported by the Open Fund of Hebei Cangzhou Groundwater and Land Subsidence National Observation and Research Station (CGLOS-2023-09) and the National Natural Science Foundation of China (No. 52174011). We also thank the following partners at China University of Petroleum (Beijing) for their contributions: Min Zhang and Houze Chen.

Data Availability Statement: All relevant data are within the paper.

Conflicts of Interest: The authors declare no conflict of interest.

References

1. Zhong, C.; Hou, D.; Liu, B.; Zhu, S.; Wei, T.; Gehman, J.; Alessi, D.S.; Qian, P.-Y. Water footprint of shale gas development in china in the carbon neutral era. *J. Environ. Manag.* **2023**, *331*, 117238. [CrossRef]
2. Ma, Z.; Pi, G.; Dong, X.; Chen, C. The situation analysis of shale gas development in China-based on Structural Equation Modeling. *Renew. Sustain. Energy Rev.* **2017**, *67*, 1300–1307. [CrossRef]
3. Masłowski, M.; Labus, M. Preliminary Studies on the Proppant Embedment in Baltic Basin Shale Rock. *Rock Mech. Rock Eng.* **2021**, *54*, 2233–2248. [CrossRef]
4. Sone, H.; Zoback, M.D. Mechanical properties of shale-gas reservoir rocks—Part 2: Ductile creep, brittle strength, and their relation to the elastic modulus. *Geophysics* **2013**, *78*, D390–D399. [CrossRef]
5. Zheng, D.; Miska, S.; Ozbayoglu, E. The Influence of Formation Creeping on Wellbore Integrity. In Proceedings of the SPE 2021 Symposium Compilation, Virtual, 26 November 2021. [CrossRef]
6. Guo, J.; Liu, Y. Modeling of Proppant Embedment: Elastic Deformation and Creep Deformation. In Proceedings of the SPE International Production and Operations Conference & Exhibition, SPE-157449-MS, Doha, Qatar, 14–16 May 2012.

7. Katende, A.; Allen, C.; Rutqvist, J.; Nakagawa, S.; Radonjic, M. Experimental and numerical investigation of proppant embedment and conductivity reduction within a fracture in the Caney Shale, Southern Oklahoma, USA. *Fuel* **2023**, *341*, 127571. [CrossRef]
8. Katende, A.; O'Connell, L.; Rich, A.; Rutqvist, J.; Radonjic, M. A comprehensive review of proppant embedment in shale reservoirs: Experimentation, modeling and future prospects. *J. Nat. Gas Sci. Eng.* **2021**, *95*, 104143. [CrossRef]
9. Chang, C.; Zoback, M.D. Viscous creep in room-dried unconsolidated Gulf of Mexico shale (I): Experimental results. *J. Pet. Sci. Eng.* **2009**, *69*, 239–246. [CrossRef]
10. Rassouli, F.S.; Zoback, M.D. Comparison of Short-Term and Long-Term Creep Experiments in Shales and Carbonates from Unconventional Gas Reservoirs. *Rock Mech. Rock Eng.* **2018**, *51*, 1995–2014. [CrossRef]
11. Sone, H.; Zoback, M.D. Time-dependent deformation of shale gas reservoir rocks and its long-term effect on the in situ state of stress. *Int. J. Rock Mech. Min. Sci.* **2014**, *69*, 120–132. [CrossRef]
12. Borja, R.I.; Yin, Q.; Zhao, Y. Cam-Clay plasticity. Part IX: On the anisotropy, heterogeneity, and viscoplasticity of shale. *Comput. Methods Appl. Mech. Eng.* **2020**, *360*, 112695. [CrossRef]
13. Chang, C.; Zoback, M.D. Viscous creep in room-dried unconsolidated Gulf of Mexico shale (II): Development of a viscoplasticity model. *J. Pet. Sci. Eng.* **2010**, *72*, 50–55. [CrossRef]
14. Darabi, M.K.; Abu Al-Rub, R.K.; Masad, E.A.; Huang, C.-W.; Little, D.N. A modified viscoplastic model to predict the permanent deformation of asphaltic materials under cyclic-compression loading at high temperatures. *Int. J. Plast.* **2012**, *35*, 100–134. [CrossRef]
15. Kabwe, E.; Karakus, M.; Chanda, E.K. Creep constitutive model considering the overstress theory with an associative viscoplastic flow rule. *Comput. Geotech.* **2020**, *124*, 103629. [CrossRef]
16. Haghighat, E.; Rassouli, F.S.; Zoback, M.D.; Juanes, R. A viscoplastic model of creep in shale. *Geophysics* **2020**, *85*, MR155–MR166. [CrossRef]
17. Ding, X.; Zhang, F.; Zhang, G. Modelling of time-dependent proppant embedment and its influence on tight gas production. *J. Nat. Gas Sci. Eng.* **2020**, *82*, 103519. [CrossRef]
18. Fan, M.; Han, Y.; Chen, C. Thermal–Mechanical Modeling of a Rock/Proppant System to Investigate the Role of Shale Creep on Proppant Embedment and Fracture Conductivity. *Rock Mech. Rock Eng.* **2021**, *54*, 6495–6510. [CrossRef]
19. Liu, Y.; Mu, S.; Guo, J.; Yang, X.; Chen, C.; Liu, H. Analytical model for fracture conductivity with multiple particle sizes and creep deformation. *J. Nat. Gas Sci. Eng.* **2022**, *102*, 104607. [CrossRef]
20. Luo, Z.; Zhang, N.; Zhao, L.; Liu, F.; Liu, P.; Li, N. Modeling of pressure dissolution, proppant embedment, and the impact on long-term conductivity of propped fractures. *J. Pet. Sci. Eng.* **2020**, *186*, 106693. [CrossRef]
21. Geng, Z.; Bonnelye, A.; David, C.; Dick, P.; Wang, Y.; Schubnel, A. Pressure Solution Compaction during Creep Deformation of Tournemire Shale: Implications for Temporal Sealing in Shales. *J. Geophys. Res. Solid Earth* **2021**, *126*, e2020JB021370. [CrossRef]
22. Yin, Q.; Liu, Y.; Borja, R.I. Mechanisms of creep in shale from nanoscale to specimen scale. *Comput. Geotech.* **2021**, *136*, 104138. [CrossRef]
23. Rafieepour, S.; Zheng, D.; Miska, S.; Ozbayoglu, E.; Takach, N.; Yu, M.; Zhang, J. Combined Experimental and Well Log Evaluation of Anisotropic Mechanical Properties of Shales: An Application to Wellbore Stability in Bakken Formation. In Proceedings of the SPE Annual Technical Conference and Exhibition, Virtual, 21–22 October 2020. [CrossRef]
24. Zheng, D.; Ozbayoglu, E.; Miska, S.; Zhang, J. Combined Experimental and Well Log Study of Anisotropic Strength of Shale. In Proceedings of the SPE Annual Technical Conference and Exhibition, San Antonio, TX, USA, 16–18 October 2023. [CrossRef]
25. Zheng, D.; Ozbayoglu, E.; Miska, S.; Zhang, J. Experimental Study of Anisotropic Strength Properties of Shale. In Proceedings of the 57th U.S. Rock Mechanics/Geomechanics Symposium, Atlanta, GA, USA, 15–28 June 2023. [CrossRef]
26. Hartley, P. Introduction to Computational Plasticity. *J. Phys. A Math. Gen.* **2006**, *39*, 3850. [CrossRef]
27. Lazari, M.; Sanavia, L.; di Prisco, C.; Pisanò, F. Predictive potential of Perzyna viscoplastic modelling for granular geomaterials. *Int. J. Numer. Anal. Methods Geomech.* **2019**, *43*, 544–567. [CrossRef]
28. Perzyna, P. Fundamental Problems in Viscoplasticity. *Adv. Appl. Mech.* **1966**, *9*, 243–377. [CrossRef]
29. Song, F.; Rodriguez-Dono, A.; Olivella, S. Hydro-mechanical modelling and analysis of multi-stage tunnel excavations using a smoothed excavation method. *Comput. Geotech.* **2021**, *135*, 104150. [CrossRef]
30. Wang, X.; Wang, L.B.; Xu, L.M. Formulation of the return mapping algorithm for elastoplastic soil models. *Comput. Geotech.* **2004**, *31*, 315–338. [CrossRef]
31. Wang, J. Mechanical Properties and Researches of Roadway Supporting Technology of Oil Shale Under the Action of Water. Ph.D. Thsis, Liaoning University of Technology, Jinzhou, China, 2012.